DOI: 10.1002/ ((please add manuscript number))

Article type: Full Paper

Visualizing Non-Radiative Mobile Defects in Organic-Inorganic Perovskite Materials

*Olivia Hentz, Akshay Singh, Zhibo Zhao, and Silvija Gradečak**

O. Hentz, A. Singh, Z. Zhao, Prof. S. Gradečak

Department of Materials Science and Engineering

Massachusetts Institute of Technology

77 Massachusetts Ave.

Cambridge, MA 02139, USA
E-mail: gradecak@mit.edu

Keywords: organic-inorganic perovskites, point defect migration, photoluminescence, lateral devices

Organic-inorganic perovskite materials have mobile charged point defects that migrate in response to voltage biasing and illumination, causing device performance variation over time. Further improvements in device stability and reliability require methods to visualize point defect migration, estimate ionic mobilities, and identify factors influencing their migration. In this work, we demonstrate a versatile method to track the migration of non-radiative point defects *in-situ*. We

used photoluminescence mapping of laterally biased perovskite films to track continuous changes in non-radiative recombination as charge-trapping defects migrate between the device electrodes. We developed a Monte Carlo framework of defect drift and diffusion that is consistent with experimental photoluminescence observations, which combined enabled us to estimate point defect mobilities in methylammonium lead iodide films. Furthermore, measurements performed on materials with varied grain sizes demonstrate that point defect mobility is 1500× faster at grain boundaries compared to bulk. These findings imply that grain morphology can be used to tune point defect mobility such that large-grained or single-crystal materials inhibit point defect migration. The methods used in this work can be applied to visualize and quantify the migration of charge-trapping point defects in a wide range of state-of-the-art perovskite materials targeted toward reduced ionic mobilities and superior device stability.

1. Introduction

Organic-inorganic perovskite solar cells (PSCs) have received significant interest in recent years due to their low cost, light weight, easy processability, and rapid rise in power conversion efficiency approaching that of modern silicon solar cells.[1,2] However, future commercialization and practical applications require addressing critical limitations posed by material degradation and inconsistent device performance. In particular, charged point defects in perovskite materials likely play a role in the electronic behavior of PSCs;[3] device stability under moisture, oxygen, voltage biasing and illumination;[4–9] and the reliability of device performance under varied operating conditions.[10]

Although it has become increasingly accepted that charged point defects (or ions) migrate in perovskite materials under illumination or voltage biasing,[11–14] the nature of these mobile species in terms of their mobility, energy levels, and charge remains poorly understood. To address these questions, lateral device structures (in which both electrodes are on the same side of the perovskite film, spaced by hundreds of microns) (**Figure 1**a) have been used to successfully identify the existence of mobile ions[11] and track the effects of point defect migration in perovskite thin films *via* compositional changes, doping effects, and degradation.[15–17] However, most of these studies suffer from material degradation during the measurement and do not allow for continuous tracking of changes *in-situ* due to inherent characterization technique limitations.

In this work, we develop an approach that enables direct, *in-situ* tracking of mobile non-radiative point defects in PSC materials without degradation, from which their mobility and charge can be estimated. We then identify film properties correlated with increased (or decreased) point defect migration rates. The measurements are based on time-dependent photoluminescence (PL) mapping of polycrystalline films of varied morphology in a laterally biased geometry. We demonstrate that localized, time-dependent enhancement in PL intensity provides effective visualization of the removal of point defects under applied device biasing. In controlling for film degradation, we also reveal adverse effects of metal migration from the electrodes into PSC films and identify chromium as a suitable electrode material for the lateral biasing measurements. We further correlate the spatio-temporal evolution of PL intensity to defect charge and mobility through Monte Carlo drift-diffusion simulations of defect migration. Finally, we demonstrate the role of grain morphology in point defect migration by providing evidence for enhanced point defect mobility at grain boundaries.

2. Photoluminescence mapping of lateral devices

2.1. Measurement set-up

To study changes in radiative recombination under lateral voltage biasing, we developed a system for PL mapping with ~5 µm resolution over regions that are hundreds of microns in size (**Figure 1)**. Methylammonium lead iodide ($CH_3NH_3PbI_3$) films were deposited on lateral electrodes spaced by 150 – 250 µm (**Figure 1**a), with 12 V biasing across the electrodes (see Supporting Information and Figure S1 for details on sample fabrication). As shown in **Figure 1**b, samples were illuminated with a 450 nm light emitting diode (LED), focused to a spot size of ~275 µm using a 10× microscope objective. The resulting luminescence and back-reflected light were then passed through a 600 nm long pass filter to isolate bandgap energy luminescence (~760 nm) and to remove any contribution from light reflection. The luminescence was then focused on the entrance slit of the spectrometer (set in the non-dispersive mode), followed by a charge coupled device, thus forming a PL image of the illuminated region. PL images were obtained using relatively short 1-10 s exposure time and are not expected to be impacted by the luminescence enhancement through light soaking effects observed at longer time scales.[9,18] Additionally, because only wavelengths longer than 600 nm are collected, contributions from lead iodide (expected around 510-590 nm[19]) are eliminated before reaching the spectrometer, as confirmed by using the spectrometer in dispersive mode (Supporting Information, Figure S2). We note that the PL exposure time – which is already relatively short compared to the timescale of hours over which PL changes are measured – governs the temporal resolution of this approach and could be further reduced by increasing sensitivity of the PL detector.

In accordance with previous lateral device studies, we first used gold contacts to bias the perovskite films. When encapsulated with a thin layer of poly(methyl methacrylate) (PMMA), gold-contacted samples initially showed an anomalous increase in luminescence between the biased electrodes that has not been previously reported for perovskite thin films (**Figure 2**a). This PL increase was also associated with increasingly inhomogeneous luminescence intensity across the biased region. The luminescence intensity quickly dropped with extended biasing, suggesting potential film degradation. Therefore, to understand the mechanism of the observed luminescence enhancement, it is critical to identify and control the sources of film degradation.

2.2. Controlling for degradation

To control for damage from external sources (e.g. moisture and oxygen) and eliminate potential degradation pathways, lateral biasing measurements were tested under a range of environmental conditions. We independently varied biasing atmosphere (ambient or nitrogen), electrode material (gold or chromium), and the use of PMMA encapsulation layer. As mentioned above, samples biased with gold contacts and sealed with PMMA showed PL enhancement, but with evidence of possible degradation (**Figure 2**a), likely due to migration of gold into the perovskite film. Indeed, gold has been shown to migrate through the electron transport layer of full PSC devices and into the perovskite layer under voltage biasing.[20] Since the degradation in organic-inorganic perovskite films has been shown to propagate from damaged regions,[6] damage from small amounts of gold migration could result in accelerated degradation across the entire film. Thus, to avoid the impact of metal migration on material quality and thin film PL, we used chromium electrodes which do not interact (diffuse)[20] with the perovskite films.

Figure 2b-c show that biasing of the lateral devices with chromium contacts in the absence of a PMMA capping layer, both in an inert environment or in ambient conditions, results in minimal to no PL enhancement (**Figure 2**b-c), likely due to the formation of extrinsic defects and degradation into PbI_2.[4] Starting at the positive electrode, non-encapsulated devices turned yellow under biasing, indicative of PbI_2 formation. However, films coated with PMMA and biased using chromium electrodes did not show degradation, but instead demonstrated continuous increase in PL between the two electrodes over extended periods of voltage biasing (**Figure 2**c). Visual signs of degradation were not observed in these encapsulated, chromium electrode devices during the period of PL enhancement. This result is significant as most of previous studies on laterally biased perovskite thin films have used gold contacts and reported effects of degradation.[11,15,21] We identified chromium electrodes that, together with control of external sources of degradation, enable effective tracking of the spatio-temporal PL evolution across laterally biased perovskite films, as shown in **Figure 2**c.

3. Results

3.1. Spatio-temporal photoluminescence evolution

The time evolution of PL between laterally biased electrodes can be clearly visualized by averaging the PL intensity along the length of the electrodes, indicated as the y-direction in **Figure 2**, at each time step (**Figure 3**a-b). Normalization of these experimental results to non-biased control regions to account for variations in the excitation source is explained in the Supporting Information. In all samples, the PL enhancement begins at one or both electrodes and then advances across the film towards the opposite electrode. To explain the observed PL evolution under lateral biasing and

its variation across different samples, we propose the following model based on migration of non-radiative point defects. When perovskite films are biased at low voltages, charged point defects migrate according to the applied electric field and are eventually swept out of the region between the electrodes. The removal of point defects, which act as trap states, decreases non-radiative recombination locally and causes an increase in radiative recombination and PL intensity. Therefore, variations in PL evolution across samples can be attributed to differences in the presence and mobility of specific point defect species.

3.2. Monte Carlo Simulations

To test this hypothesis and estimate the mobility and charge of migrating point defects, we formulated a Monte Carlo framework incorporating both drift and diffusion of charged defects under the biasing conditions used in this study. The resulting distribution of defects over time under voltage biasing was compared to the experimentally measured PL evolution by correlating decreased defect concentrations with increased luminescence intensity.

The Monte Carlo simulations were constructed in Python and initialized with a one-dimensional model sample (analogous to the experimental results in **Figure 3**a-b) having a random distribution of point defects along its length. The movement of defects under voltage biasing was then implemented by updating the position of each defect along the sample at one hour time steps. Individual defect movement was calculated as the sum of defect diffusion and drift over the one hour time interval. The length and direction of diffusion steps were randomly selected for each defect from a Gaussian distribution centered at zero with a standard deviation of $\sqrt{2Dt}$, where D is

the defect diffusivity calculated from the defect mobility. The length and direction of drift steps were given as:

$$\Delta x = \frac{\mu * V * t * q}{d} \quad (1)$$

where μ is the defect mobility in units of $(cm^2V^{-1}sec^{-1})$ and was used as the fitting parameter to match the experimental data. *V* is the applied voltage (12 V), t is the time corresponding to each update step (1 h), q is the sign of the charge of the migrating defect (±1), and d is the electrode spacing. Electrode spacing (and therefore position) was based on the experimental values, and drift steps were only applied to defects with positions between the electrodes. Videos showing the simulated evolution of defect distributions over time are available online as part of the Supporting Information.

Although the general PL behavior among different samples can vary, the majority of samples exhibited experimental PL characteristics similar to those shown in **Figure 3**a. In these samples, PL intensity begins to increase at the negative electrode, and then continues across the sample towards the positive electrode. This simple evolution in PL can be qualitatively described using the Monte Carlo simulations with only one negatively charged defect. For the sample shown in **Figure 3**a, Monte Carlo simulations using mobility of 2.5×10^{-11} $cm^2V^{-1}s^{-1}$ most closely match the experimental PL results (**Figure 3**c). The accuracy of this estimated mobility can be evaluated self-consistently by comparing simulation results for other mobility values, as shown in Supporting Information Figure S4; we find that qualitatively comparing the simulation and experimental results gives a mobility value robust within a factor of two.

In contrast to the commonly observed one-defect results shown in **Figure 3**a,c, the evolution of PL intensity was significantly more complex in a limited number of samples and could not be modeled effectively with only one defect species, suggesting the presence of several different mobile defect species. The origin of these additional defect species is under investigation but may be related to subtle differences in the precursor material quality or processing environment. **Figure 3**b shows one such sample that required at least four non-radiative mobile defects, two positively charged and two negatively charged with mobilities ranging from 10^{-10} to 10^{-11} $cm^2V^{-1}s^{-1}$, to model the observed PL evolution (See Supporting Information S3 for full PL maps and corresponding variation in PL intensity in non-biased regions). Given the increased number of variables used to simulate multiple defects in these films, electrodes with two different spacings were measured and mobilities and defect concentrations were selected to match both sets of PL data. The mobility and relative concentration of these four defects were estimated by iterating the modeling parameters to match the experimental results, as shown in Supporting Information, Figure S5. For comparison, in Supporting Information, Figure S5, we also show the results for a device that required three defect species for successful description.

3.3. Grain boundary effects

The estimated mobilities obtained by the Monte Carlo simulations are in agreement with theoretical and experimental reports of charged point defect mobilities in the range between 10^{-9} and 10^{-11} $cm^2 V^{-1}s^{-1}$.[12,22–26] It has previously been reported that defect mobilities may be enhanced at grain boundaries,[3,27,28] which could potentially explain the wide range of reported point defect mobilities. Therefore, to assess the role of varied grain morphology on the defect mobilities, we next

engineered films with different grain sizes, measured their PL evolution, and included grain boundary parameters in the Monte Carlo simulations.

Grain size control was achieved through annealing conditions, with thermal annealing generating small grains (~125 nm diameter) and solvent annealing (annealing with small amount of dimethylformamide vapor) generating larger grains (~255 nm diameter) (**Figure 4**a,b).[29] Next, the same set of PL measurements as discussed above were performed in laterally-biased geometries on samples of different grain sizes. As shown in **Figure 4**c,d, the rate of PL evolution was higher for samples with smaller grains than for those with larger grains, suggesting faster point defect migration in small-grain samples. To verify whether the observed difference is consistent with the hypothesis of point defect migration facilitated by grain boundaries, we created a two-dimensional Monte Carlo framework analogous to the one-dimensional framework discussed above. In this case, one-dimensional grain boundaries were randomly placed in the two-dimensional sample (Supporting Information Figure S6). The migration of defects was then defined by three mobilities: in-grain mobility, mobility along a grain boundary, and mobility perpendicular to grain boundaries (capturing effects related to defects "escaping" grain boundaries), with the first applicable to defects outside grain boundaries and the last two applicable to defects inside a grain boundary. Given the higher computational complexity of these simulations, we considered only samples exhibiting PL evolution characteristic of one mobile defect type (negatively charged defect with in-grain mobility of 1.4×10^{-12} $cm^2V^{-1}s^{-1}$, optimized to fit the experimental results for both grain sizes). Additionally, the amount of time represented by each update step was reduced to 5 min to account for the smaller length scales relevant when considering grain boundary effects.

We observe that grain size can significantly impact the reported defect mobilities in laterally biased samples. Fitting our simulations (**Figure 4**e,f) to the experimental data (**Figure 4**b,c) required mobilities 1500× faster at grain boundaries, and 100× slower perpendicular to grain boundaries, when compared with in-grain mobilities. This degree of mobility enhancement is not unprecedented; for example, oxygen diffusivity has been found to be 3-4 orders of magnitude greater at grain boundaries than in grains in Y-doped ZrO_2.[30] Comparison of these results to our one-dimensional simulations, which reveal the weighted average defect mobility (accounting collectively for the three mobilities defined above), suggests that for samples with small grains (~125 nm), the presence of grain boundaries increases the observed (average) defect mobility by one order of magnitude over the in-grain mobility.

4. Discussion

The identity of the defect species observed in this work is under investigation, but these results suggest that there are at least four possible mobile defect species that can serve as non-radiative recombination centers. Although the majority of defects with low formation energies are expected to have shallow energy levels, theoretical calculations suggest that positively charged I_{MA} and I_{Pb} antisite defects and negatively charged lead interstitials and Pb_I antisite defects are expected to have mid-gap energy levels and therefore may act as trap states.[31] Additionally, it is suspected that iodide vacancies or interstitials, and Pb_{MA} antisites at the surface of perovskite films may have deep energy levels, depending on the surface termination.[32] Although defect types and concentrations are expected to be highly dependent on synthesis conditions, iodide vacancies and interstitials are predicted to have relatively low formation energies. Therefore, iodide interstitials are most likely to account for the negative defect species observed in all samples discussed in this

work.[31,33] Finally, it remains possible that external defects, introduced by contamination of precursor materials or interaction with moisture or oxygen in the air, may act as trap states.[4,34]

The processing methods used to control grain size could cause additional differences in these films, such as differences in the concentration of various point defect species. Samples with a higher density of grain boundaries are also likely to have a higher density of trap states, illustrated in the extreme case by the low trap state densities reported for single crystals.[35] However, most measurements of trap state densities are unable to differentiate between grain boundary effects and in-grain defect concentrations. Future research should therefore aim at understanding the effect of in-grain defect concentrations as well as grain boundary disorder on differences in defect mobility for samples of varied morphology.

Regardless of the exact point defect species and concentrations responsible for the PL evolution in perovskite films, these results indicate that it is critical to take into account grain morphology when studying the mobility of defects in organic-inorganic perovskite materials. Additionally, the dependence of point defect mobility on grain morphology may help explain the decrease in observed hysteresis for high performance perovskite films, which are made of large grains and therefore have minimal grain boundaries.[36–38] Finally, hysteresis reduction with grain boundary passivation may be related to a decrease in mobility of defects at passivated grain boundaries.[39]

4. Conclusion

In conclusion, we have developed an approach for direct tracking of non-radiative point defect migration in organic-inorganic perovskite materials that is based on direct correlation

between PL intensity measurements in laterally-biased devices and Monte Carlo simulations. We first identified critical parameters for preventing degradation during the measurement, demonstrating the importance of Cr contacts and PMMA encapsulation. We then correlated PL time evolution between the electrodes with expected changes in defect distribution under voltage biasing using a drift-diffusion Monte Carlo framework. Finally, we demonstrate a 1500× enhancement in point defect mobility in grain boundaries, indicating that understanding the effects of grain size is critical in comparing mobility measurements across varied perovskite films.

The samples used in this study were based on the simplest organic-inorganic perovskite material, methylammonium lead iodide, but these methods can be applied to understanding the role of native point defects in non-radiative recombination for more complicated, state-of-the-art perovskite materials based on multiple cation and anion species. These methods can also be used to further assess the importance of point defects to the radiative quality of perovskite thin films, which is critical to the advancement of perovskite materials for a variety of applications including light emitting diodes,[40] solar cells,[41] and lasers.[42] The simple and inexpensive technique presented here has the potential to facilitate high throughput evaluation of novel film morphologies, compositions, and passivation techniques in the continued development of novel perovskite materials.

Supporting Information

Supporting Information is available from the Wiley Online Library or from the author.

Acknowledgements

This work was supported by Eni S.p.A. under the Eni-MIT Alliance Solar Frontiers Center. O.H. acknowledges graduate fellowship support through the National Science Foundation Graduate Research Fellowship under Grant No. 1122374. This work made use of the MRSEC Shared Experimental Facilities at MIT, supported by the National Science Foundation under award number DMR-1419807, and of the ONE Lab facilities at MIT. Any opinion, findings, and conclusions or recommendations expressed in this material are those of the authors and do not necessarily reflect the views of the National Science Foundation.

Received: ((will be filled in by the editorial staff))
Revised: ((will be filled in by the editorial staff))
Published online: ((will be filled in by the editorial staff))

References:

[1] "National Renewable Energy Laboratory, Best Research-Cell Efficiencies chart," can be found under www.nrel.gov/ncpv/images/efficiency_chart.jpg, accessed: April 2018.

[2] J.-P. Correa-Baena, A. Abate, M. Saliba, W. Tress, T. Jesper Jacobsson, M. Grätzel, A. Hagfeldt, *Energy Environ. Sci.* **2017**, *10*, 710.

[3] O. Hentz, P. H. Rekemeyer, S. Gradečak, *Adv. Energy Mater.* **2018**, 1701378.

[4] N. Aristidou, C. Eames, I. Sanchez-Molina, X. Bu, J. Kosco, M. S. Islam, S. A. Haque, *Nat. Commun.* **2017**, *8*, 15218.

[5] T. Handa, D. M. Tex, A. Shimazaki, T. Aharen, A. Wakamiya, Y. Kanemitsu, *Opt. Express* **2016**, *24*, A917.

[6] A. Merdasa, M. Bag, Y. Tian, E. Källman, A. Dobrovolsky, I. G. Scheblykin, *J. Phys. Chem. C* **2016**, *120*, 10711.

[7] D. Bryant, N. Aristidou, S. Pont, I. Sanchez-Molina, T. Chotchunangatchaval, S. Wheeler, J. R. Durrant, S. A. Haque, *Energy Environ. Sci.* **2016**, *9*, 1655.

[8] K. Domanski, B. Roose, T. Matsui, M. Saliba, S.-H. Turren-Cruz, J.-P. Correa-Baena, C. R. Carmona, G. Richardson, J. M. Foster, F. De Angelis, J. M. Ball, A. Petrozza, N. Mine, M. K. Nazeeruddin, W. Tress, M. Grätzel, U. Steiner, A. Hagfeldt, A. Abate, *Energy Environ. Sci.* **2017**, *10*, 604.

[9] D. W. DeQuilettes, W. Zhang, V. M. Burlakov, D. J. Graham, T. Leijtens, A. Osherov, H. J. Snaith, D. S. Ginger, S. D. Stranks, *Nat. Commun.* **2016**, *7*, 11683.

[10] N. Pellet, F. Giordano, M. I. Dar, G. Gregori, S. M. Zakeeruddin, J. Maier, M. Grätzel, *Prog. Photovolt Res. Appl.* **2017**, *25*, 942.

[11] Z. Xiao, Y. Yuan, Y. Shao, Q. Wang, Q. Dong, C. Bi, P. Sharma, A. Gruverman, J. Huang, *Nat. Mater.* **2015**, *14*, 193.

[12] C. Eames, J. M. Frost, P. R. F. Barnes, B. C. O'Regan, A. Walsh, M. S. Islam, *Nat. Commun.* **2015**, *6*, 7497.

[13] P. Calado, A. M. Telford, D. Bryant, X. Li, J. Nelson, C. Brian, O. Regan, P. R. F. Barnes, *Nat. Commun.* **2016**, *7*, 13831.

[14] O. Hentz, Z. Zhao, S. Gradečak, *Nano Lett.* **2016**, *16*, 1485.

[15] T. Leijtens, E. T. Hoke, G. Grancini, D. J. Slotcavage, G. E. Eperon, J. M. Ball, M. De Bastiani, A. R. Bowring, N. Martino, K. Wojciechowski, M. D. McGehee, H. J. Snaith, A. Petrozza, *Adv. Energy Mater.* **2015**, *5*, 1500962.

[16] C. Li, A. Guerrero, Y. Zhong, A. Gräser, C. A. M. Luna, J. Köhler, J. Bisquert, R. Hildner, S. Huettner, *Small* **2017**, *13*, 1.

[17] Y. Yuan, Q. Wang, Y. Shao, H. Lu, T. Li, A. Gruverman, J. Huang, *Adv. Energy Mater.* **2016**, *6*, 1501803.

[18] C. Zhao, B. Chen, X. Qiao, L. Luan, K. Lu, B. Hu, *Adv. Energy Mater.* **2015**, *5*, 1500279.

[19] J. F. Condeles, R. A. Ando, M. Mulato, *J. Mater. Sci.* **2008**, *43*, 525.

[20] K. Domanski, J. P. Correa-Baena, N. Mine, M. K. Nazeeruddin, A. Abate, M. Saliba, W. Tress, A. Hagfeldt, M. Grätzel, *ACS Nano* **2016**, *10*, 6306.

[21] Y. Yuan, J. Chae, Y. Shao, Q. Wang, Z. Xiao, A. Centrone, J. Huang, *Adv. Energy Mater.* **2015**, *5*, 1.

[22] O. Almora, A. Guerrero, G. Garcia-Belmonte, *Appl. Phys. Lett.* **2016**, *108*, 7.

[23] J. M. Azpiroz, E. Mosconi, J. Bisquert, F. De Angelis, *Energy Environ. Sci.* **2015**, *8*, 2118.

[24] J. Beilsten-Edmands, G. E. Eperon, R. D. Johnson, H. J. Snaith, P. G. Radaelli, *Appl. Phys. Lett.* **2015**, *106*, 173502.

[25] S. Van Reenen, M. Kemerink, H. J. Snaith, *J. Phys. Chem. Lett.* **2015**, *6*, 3808.

[26] J. Haruyama, K. Sodeyama, L. Han, Y. Tateyama, *J. Am. Chem. Soc.* **2015**, *137*, 10048.

[27] Y. Shao, Y. Fang, T. Li, Q. Wang, Q. Dong, Y. Deng, Y. Yuan, H. Wei, M. Wang, A. Gruverman, J. Shield, J. Huang, *Energy Environ. Sci.* **2016**, *9*, 1752.

[28] J. S. Yun, J. Seidel, J. Kim, A. M. Soufiani, S. Huang, J. Lau, N. J. Jeon, S. Il Seok, M. A. Green, A. Ho-Baillie, *Adv. Energy Mater.* **2016**, *6*, 1.

[29] Z. Xiao, Q. Dong, C. Bi, Y. Shao, Y. Yuan, J. Huang, *Adv. Mater.* **2014**, *26*, 6503.

[30] G. Kroner, K. Reimann, R. Rower, U. Sodervall, H.-E. Schaefer, *Proc. Natl. Acad. Sci. U. S. A.* **2003**, *100*, 3870.

[31] W.-J. Yin, T. Shi, Y. Yan, *Appl. Phys. Lett.* **2014**, *104*, 63903.

[32] H. Uratani, K. Yamashita, *J. Phys. Chem. Lett.* **2017**, *8*, 742.

[33] S. Heo, G. Seo, Y. Lee, D. Lee, M. Seol, J. Lee, J.-B. Park, K. Kim, D.-J. Yun, Y. S. Kim, J. K. Shin, T. K. Ahn, M. K. Nazeeruddin, *Energy Environ. Sci.* **2017**, *10*, 1128.

[34] J. R. Poindexter, R. L. Z. Hoye, L. Nienhaus, R. C. Kurchin, A. E. Morishige, E. E. Looney, A. Osherov, J. P. Correa-Baena, B. Lai, V. Bulović, V. Stevanović, M. G. Bawendi, T. Buonassisi, *ACS Nano* **2017**, *11*, 7101.

[35] D. Shi, V. Adinolfi, R. Comin, M. Yuan, E. Alarousu, A. Buin, Y. Chen, S. Hoogland, A. Rothenberger, K. Katsiev, Y. Losovyj, X. Zhang, P. A. Dowben, O. F. Mohammed, E. H. Sargent, O. M. Bakr, *Science (80-.).* **2015**, *347*, 519.

[36] B. Yang, O. Dyck, J. Poplawsky, J. Keum, A. Puretzky, S. Das, I. Ivanov, C. Rouleau, G. Duscher,

D. Geohegan, K. Xiao, *J. Am. Chem. Soc.* **2015**, *137*, 9210.

[37] W. S. Yang, B.-W. Park, E. H. Jung, N. J. Jeon, Y. C. Kim, D. U. Lee, S. S. Shin, J. Seo, E. K. Kim, J. H. Noh, S. Il Seok, *Science (80-.).* **2017**, *356*, 1376.

[38] W. Nie, H. Tsai, R. Asadpour, A. J. Neukirch, G. Gupta, J. J. Crochet, M. Chhowalla, S. Tretiak, M. A. Alam, H. Wang, *Science (80-.).* **2015**, *347*, 522.

[39] Y. Shao, Z. Xiao, C. Bi, Y. Yuan, J. Huang, *Nat. Commun.* **2014**, *5*, 5784.

[40] L. Zhang, X. Yang, Q. Jiang, P. Wang, Z. Yin, X. Zhang, H. Tan, Y. M. Yang, M. Wei, B. R. Sutherland, E. H. Sargent, J. You, *Nat. Commun.* **2017**, *8*, 1.

[41] W. Tress, *Adv. Energy Mater.* **2017**, *7*, DOI 10.1002/aenm.201602358.

[42] Q. Zhang, R. Su, W. Du, X. Liu, L. Zhao, S. T. Ha, Q. Xiong, *Small Methods* **2017**, *1*, 1700163.

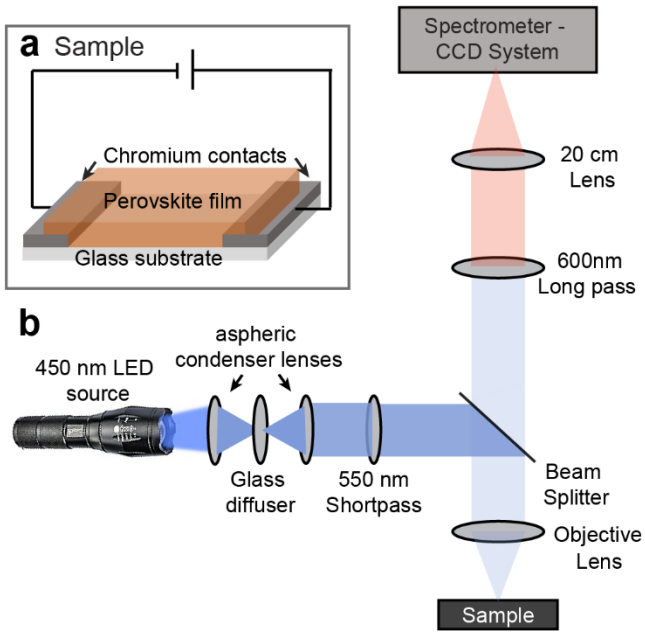

Figure 1. Schematic of (a) the laterally biased sample configuration used for PL mapping experiments. Metal contacts were deposited under the perovskite film and 12 V bias was applied over a distance of 150-250 nm. (b) Photoluminescence mapping set-up using a 450 nm LED source focused on the sample, with luminescence isolated by a long pass filter and collected by a spectrometer/CCD system.

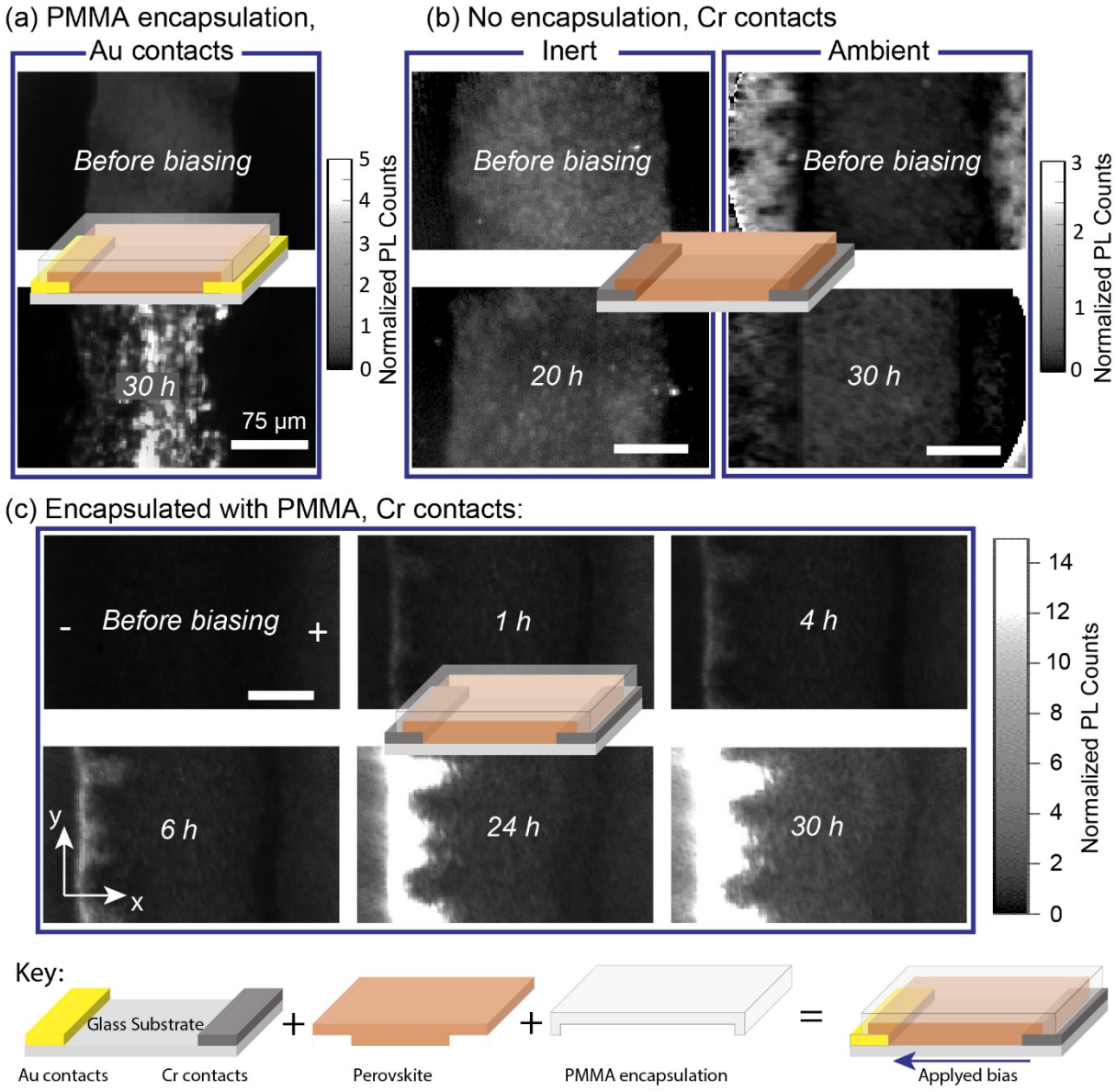

Figure 2. PL maps of laterally biased perovskite films under varied conditions. Images are normalized based by the luminescence intensity of unbiased regions of the same film. Schematics show the contacts (gold or chromium) and whether or not the sample was encapsulated with PMMA, as described in the key. (a) Films biased with gold contacts and encapsulated with PMMA. (b) Films biased with chromium contacts and exposed to inert or ambient conditions during biasing with no encapsulation. (c) Films biased with chromium contacts and encapsulated with PMMA. For all films, the negative electrode was on the left and the positive electrode was on the right. The axis shown in the bottom left image indicates the x and y directions referred to in the text.

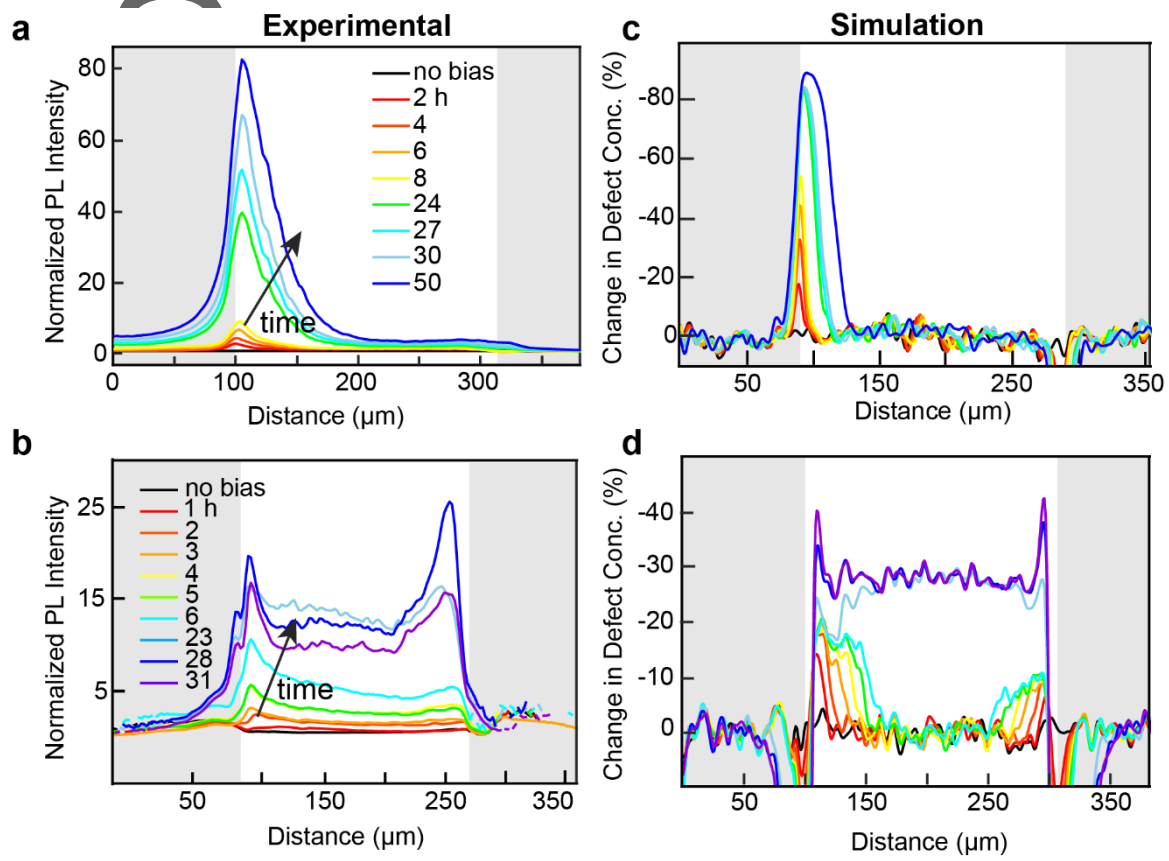

Figure 3. Average PL intensity across electrodes of laterally biased perovskite films measured at various time points during biasing, and corresponding Monte Carlo simulations. (a) Typical PL evolution (normalized by non-biased regions as explained in the Supporting Information). (b) Atypical PL evolution showing PL enhancement at both the positive and negative electrodes. (c) Monte Carlo simulation of defect distribution over time with one negative mobile defect with mobility of 5.6×10^{-11} $cm^2V^{-1}s^{-1}$. (d) Monte Carlo simulation of defect distribution over time with four mobile defects, two positive and two negative with mobilities between 10^{-10} and 10^{-11} $cm^2V^{-1}s^{-1}$. In all cases, the negative electrode is on the left and the positive electrode is on the right and approximate electrodes positions are indicated by the light grey regions.

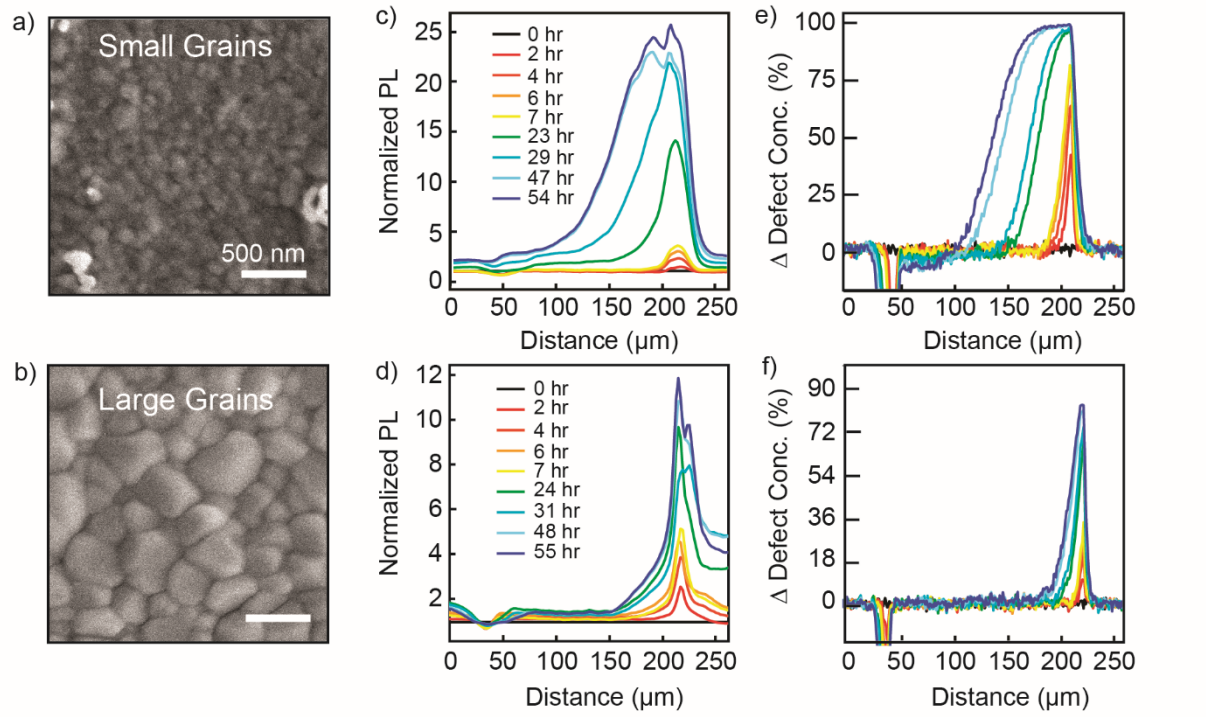

Figure 4. Dependence of PL evolution on grain size. (a,b) SEM images of perovskite films formed by (a) thermal annealing and (b) solvent annealing. (c,d) Experimental evolution of photoluminescence (averaged down the y-axis indicated in Figure 2) under voltage biasing for films shown in (a) and (b) respectively. (e,f) Simulated change in defect concentration between electrodes under voltage biasing using 2D simulations with grain sizes matching (a) and (b) respectively. In all cases, the positive electrode is on the left and the negative electrode is on the right.

Photoluminescence mapping of lateral organic-inorganic perovskite devices allows for direct tracking of mobile defects. By tracking the evolution of photoluminescence intensity increase across laterally biased organic-inorganic perovskite films, the mobility and charge of non-radiative point defects are uncovered. These methods are then used to demonstrate the degree to which grain boundaries facilitate point defect migration.

organic-inorganic perovskites, point defect migration, photoluminescence, lateral devices

O. Hentz, A. Singh, Z. Zhao, S. Gradečak*

Visualizing Non-Radiative Mobile Defects in Organic-Inorganic Perovskite Materials